NUMERICAL MODELING OF BEACH RECOVERY SEAWARD OF CLOSED KATRINA CUT IN DAUPHIN ISLAND, ALABAMA

BY

TINGTING ZHU AND NOBUHISA KOBAYASHI

RESEARCH REPORT NO. CACR-22-02
SPRING 2022

CENTER FOR APPLIED COASTAL RESEARCH

University of Delaware
Newark, Delaware 19716

ACKNOWLEDGMENTS

This study was supported by the U.S. Coastal Research Program under Agreement No. W912HZ-20-2-0016.

TABLE OF CONTENTS

LIST OF TABLES

LIST OF FIGURES

ABSTRACT

A rubble mound structure was constructed in 2011 across the 2 km wide channel breached by Hurricane Katrina in 2005. This breached channel is called Katrina Cut in Dauphin Island, Alabama. The recovery of the eroded beach seaward of the closed Katrina Cut was investigated using the numerical model CSHORE and available data during 2015-2020. The dry beach width increased more than 80 m seaward of the Katrina Cut structure and decreased up to 37 m on the neighboring beach. The computed longshore sand transport rate was of the order of 10^5 m^3/y and smaller on the recovering beach with larger water depth. The computed onshore sand transport rate was sufficient for the observed beach recovery. The recovering beach seaward of the structure reduced the depth-limited breaking wave height and wave action on the rubble mound structure during Hurricane Nate in 2017. This temporary structure triggered the recovery of the breached beach and may have become more lasting because of the increasing protection by the fronting beach.

Chapter 1

INTRODUCTION

Barrier islands are common along the coasts in the Gulf of Mexico and provide the natural barrier of the mainland coast. Morphological changes of barrier islands are mainly caused by sediment transport under normal daily waves and occasional storm surges and waves. Hurricane Katrina produced a 2 km wide breach through the uninhabited beach segment of Dauphin Island, Alabama, in 2005 (Froede 2008). This breached channel called Katrina Cut was closed with a rubble mound structure constructed in 2011 (Webb et al. 2011). Beach recovery occurred seaward of the Katrina Cut structure with the visible increase of the dry beach width during 2011 – 2020 (Gonzalez et al. 2020). Mickey et al. (2020) devised seven potential restoration measures of Dauphin Island and assessed the decadal island evolution of each measure in response to various storm and sea-level change scenarios using a long-term longshore sediment transport model, a short-term storm impact model, and an empirical dune growth model. Gonzalez et al. (2020) performed the structure response assessment of the Katrina Cut structure using a Monte Carlo life-cycle approach. The water depth in front of the structure was found to be important in estimating the breaking wave height. Coogan et al. (2019) measured subaerial geomorphic changes on Dauphin Island caused by overwash and inundation including regions near the Katrina Cut structure during Hurricane Nate in 2017. Little structure damage to the infrastructure was observed on

Dauphin Island. This study examined the long-term subaqueous sand transport and the breached beach recovery seaward of the Katrina Cut structure as well as the effect of the recovering beach on the structure stability.

Prasseri et al. (2018) used a 2DH (two dimensional in the horizontal plane) XBeach model (Roelvink et al. 2009) to examine the influence of bed friction variability on the morphodynamics of the entire Dauphin Island during Hurricanes Ivan (2004) and Katrina (2005) before the construction of the Katrina Cut structure in 2011. The cross-shore model CSHORE (Kobayashi 2016) has been compared and verified with many small-scale and large-scale laboratory and field data of sand beach evolution and dune erosion. CSHORE is efficient numerically and was used to predict beach erosion and recovery along 16 cross-shore lines spanning 5 km alongshore for the duration of 272 days (Kobayashi and Jung 2012). CSHORE predicted both erosion and accretion above the mean sea level within a factor of about 2. In this study, the duration is extended to 2161 days and CSHORE is used to predict beach recovery and erosion seaward of the closed Katrina Cut.

In the following, available field data including beach profiles, offshore wave conditions, and tide gauge data are presented in Chapter 2.

In Chapter 3, CSHORE is used to reproduce the recovery process seaward of the closed Katrina Cut under long-term constant waves. The representative waves based on the visual wave observations by Douglass (1994) are selected as incident constant waves. The sensitivity of the computed recovery results to the representative waves is discussed in this chapter.

In Chapter 4, the beach morphology and the rubble mound structure stability are assessed during a short-term major storm, Hurricane Nate. The model CSHORE can predict damage on the rubble mound by wave action.

Finally, the findings of this study are summarized in Chapter 5.

Chapter 2

AVAILABLE FIELD DATA

The topography of the closed Katrina Cut from 2015 to 2020 was analyzed using five aerial images (Google Earth Pro), as shown in Figure 2.1. The corresponding shoreline contours are depicted in Figure 2.2 in which the end day of each month is applied to count the number of days since 1 January 2015. The Mississippi Sound and the Gulf of Mexico are located north and south of Dauphin Island. The dry beach seaward of the closed Katrina Cut became wide. The net longshore sand transport on the beach facing the Gulf of Mexico is to the west (e.g., Douglass 1994). Available beach profile data, visual observations, offshore wave data, and tide gauge data in the study area are presented in the following.

2.1 Beach Profile Data

The cross-shore profiles along lines L1 – L7 of 1 km cross-shore length in Figure 2.2 were extracted from the 2015 digital elevation model (DEM) with no restoration measure released by Mickey et al. (2019). The shoreline contour of 1 January 2015 in Figure 2.2 is in agreement with the 2015 DEM shoreline based on the elevation $z = 0$ at the datum of NAVD88 (the North American Vertical Datum of 1988). Consequently, the shoreline contours of 1 January 2015 and the other four days in Figure 2.2 are assumed to be located at the elevation $z = 0$ (NAVD88) in this study. The tide effect on the shoreline location is neglected for this micro-tidal beach with a mean tidal range

of 0.36 m (NOAA 2021a). The foreshore slopes along L1 – L7 were steeper[than 1/15 (vertical/horizontal). The error of the shoreline location must be less than about 5 m. The alongshore distance between the two adjacent lines is 501.4 m.

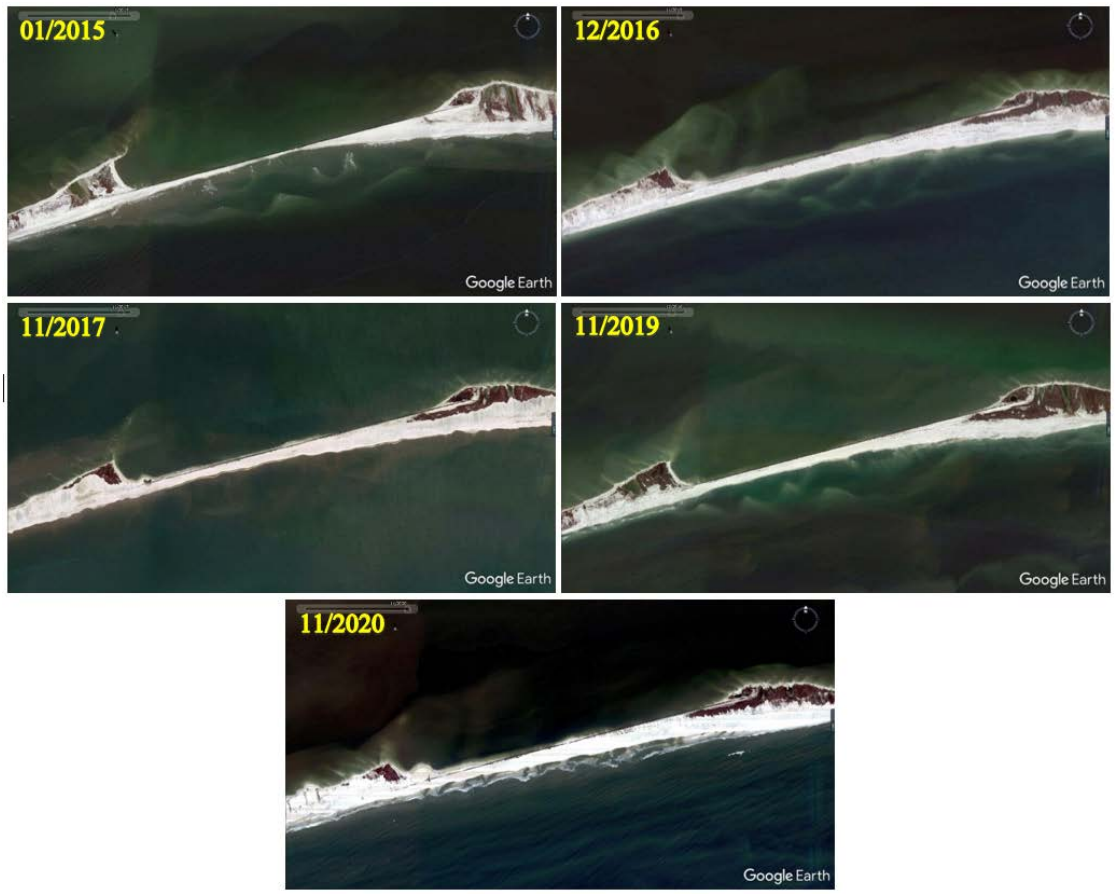

Figure 2.1 Google photos of Katrina Cut in Dauphin Island, AL from 2015 to 2020

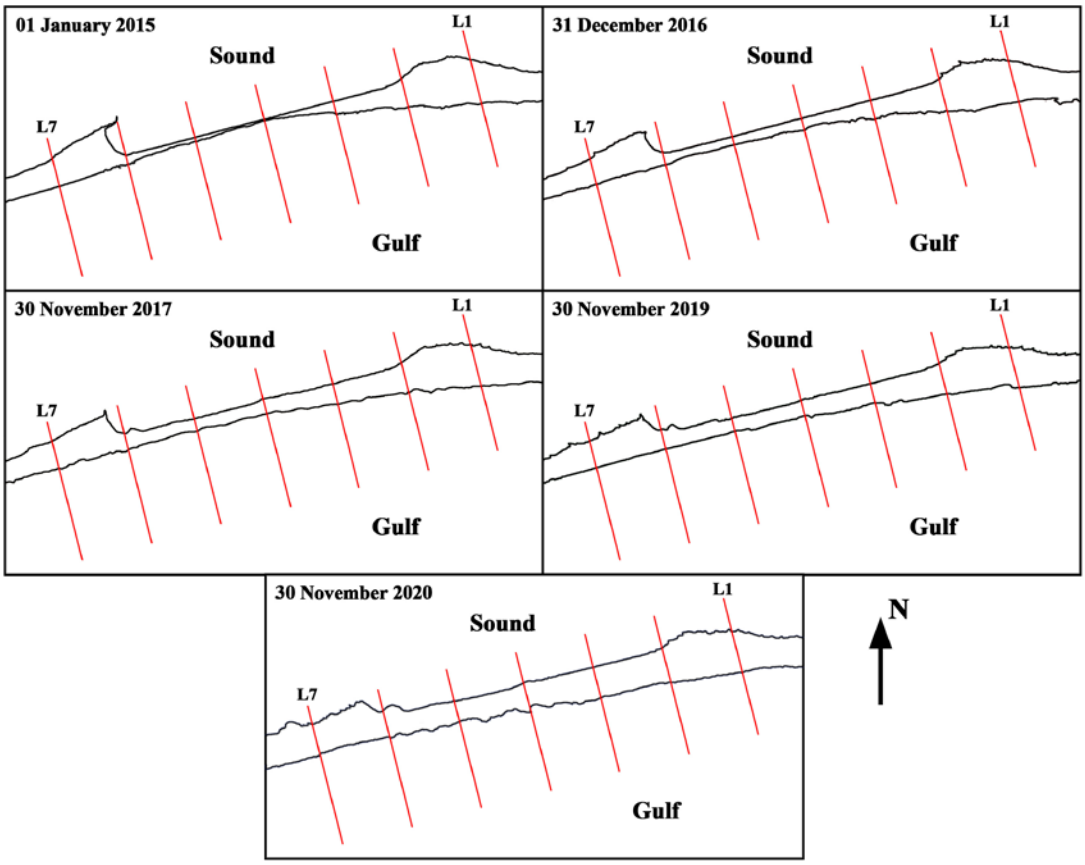

Figure 2.2 Shoreline contours in the vicinity of closed Katrina Cut in Dauphin Island, Alabama between the Gulf of Mexico and the Mississippi Sound from 2015 to 2020 and seven cross-shore lines (L1 – L7) oriented 16° counterclockwise from the north where the length of each line is 1 km

Figures 2.3 – 2.4 depict the cross-shore profiles along lines L1 – L7. The onshore coordinate x is taken as x = 0 at the seaward boundary in the water depth of about 6 m. The landward boundary of x = 1,000 m is located north of the Katrina Cut structure in the water depth of about 2 m. The alongshore coordinate is positive toward the west. The cross-shore profiles along the center lines L3 – L6 have a narrow dry beach width and a small amount of sand deposited seaward of the rubble mound structure, especially the middle line L4. However, the beach profiles along the edge lines L1, L2, and L7 have a wider dry beach width.

The shoreline contours facing the Gulf of Mexico in Figure 2.2 are used to quantify the recovery of the eroded beach along L1 – L7. The seaward displacement Δx of the shoreline from the shoreline location on 1 January 2015 is obtained as a function of the number of days since 1 January 2015 and tabulated in Table 2.1. Δx is positive for shoreline accretion and negative for shoreline erosion. The dry beach width increased up to 83 m in front of the Katrina Cut structure (L2 – L6) and decreased up to 37 m at the edges (L1 and L7) during 2015-2020.

Table 2.1 Seaward shoreline displacement Δx as a function of days since 1 January 2015 for lines L1 – L7

Date	**Number of Days**	**Seaward Shoreline Displacement Δx (m)**						
		L1	**L2**	**L3**	**L4**	**L5**	**L6**	**L7**
1 January 2015	0	0	0	0	0	0	0	0
31 December 2016	731	-14	26	25	61	18	9	-16
30 November 2017	1065	-14	4	43	57	34	11	-21
30 November 2019	1795	-4	17	35	73	36	13	-21
30 November 2020	2161	-3	29	53	83	56	23	-37

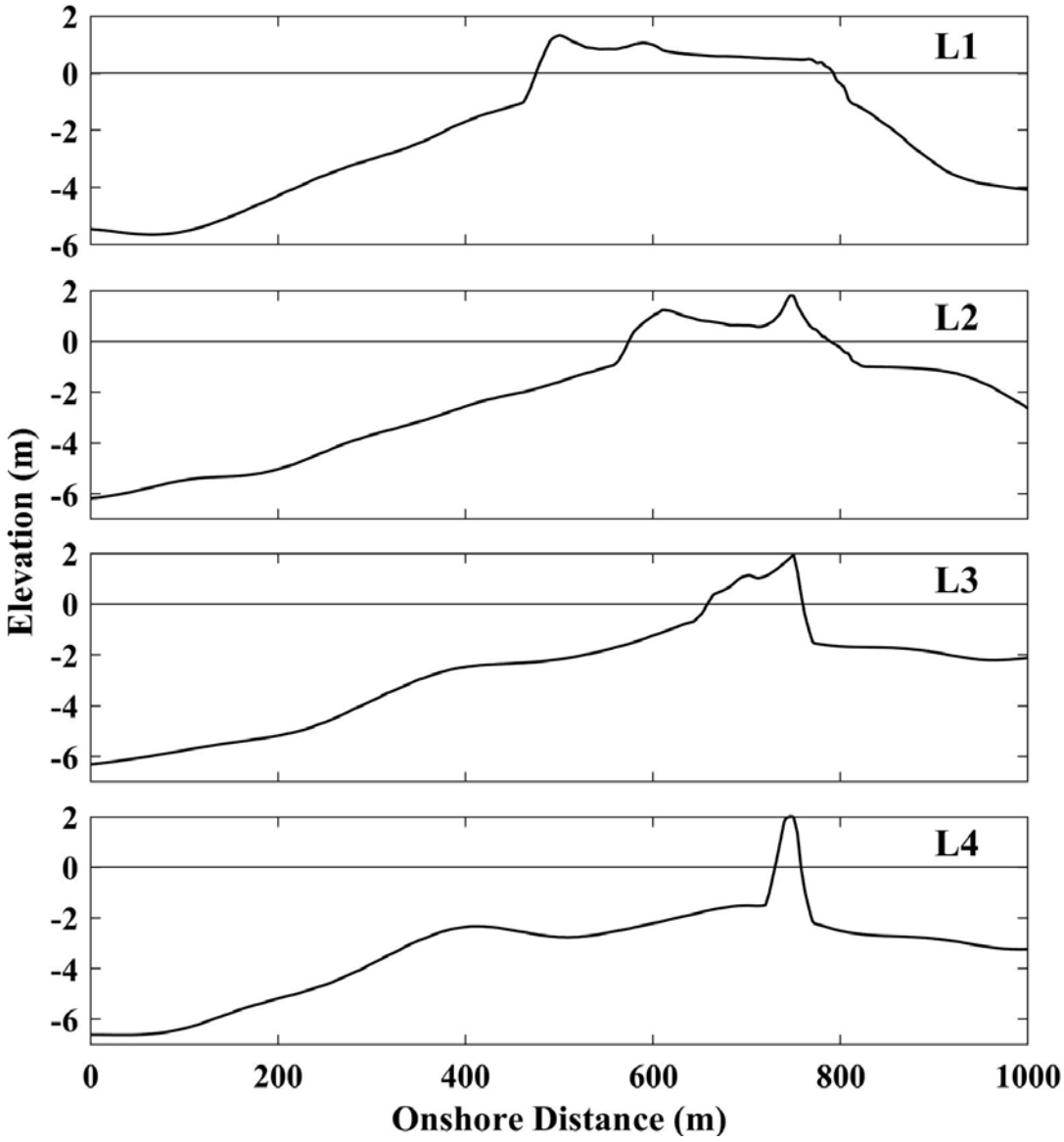

Figure 2.3 Bottom elevations along cross-shore lines L1, L2, L3, and L4

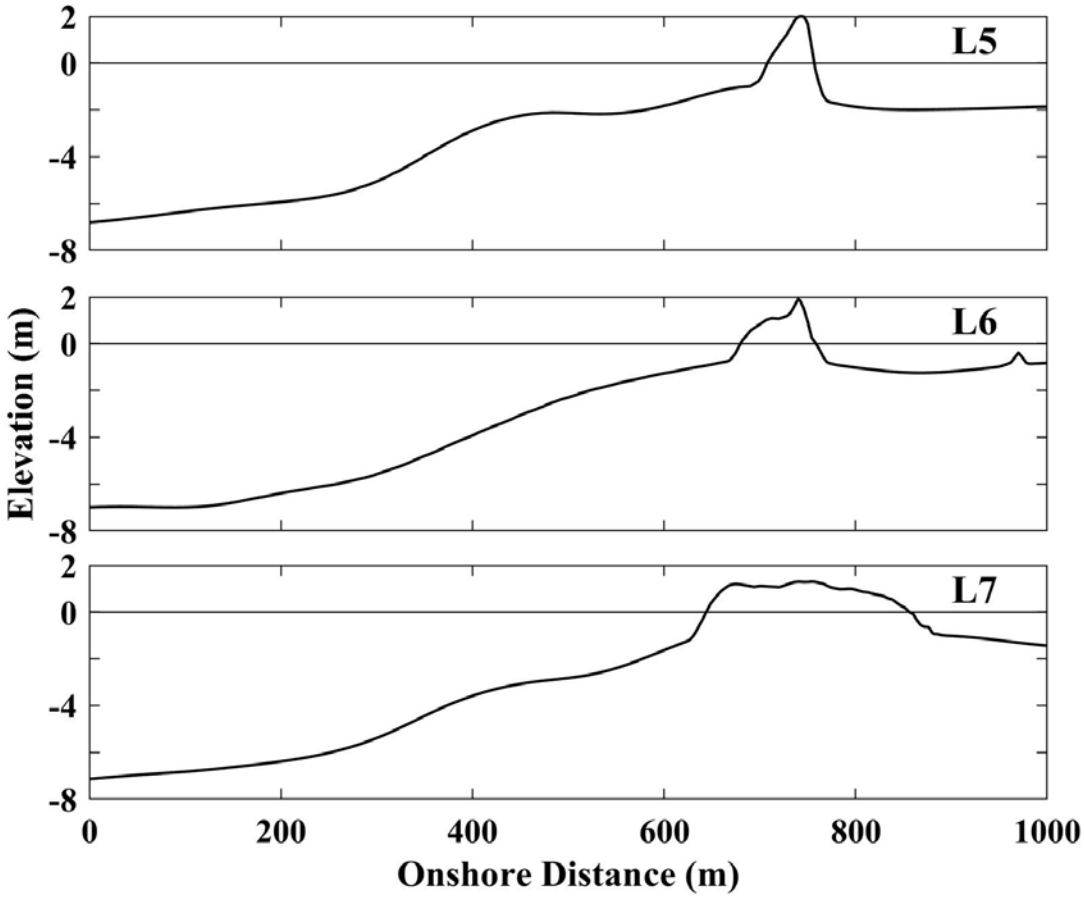

Figure 2.4 Bottom elevations along cross-shore lines L5, L6, and L7

2.2 Visual Wave Observations

Douglass (1994) performed visual wave observations and beach profile surveys during 1990 – 1991 to investigate beach erosion and accretion as well as sediment transport paths along the Gulf of Mexico beaches of Dauphin Island. The sand is well sorted near the Katrina Cut and the median diameter is approximately 0.37 mm. The net longshore sand transport is to the west. The annual longshore sand transport rate is of the order of 10^5 m^3 per year. The monthly mean wave heights, periods, and angles near the Katrina Cut are in the range of 0.4 – 0.8 m, 6 – 10 s, and 5 – 15°, respectively, where the wave angle is positive counterclockwise from the cross-shore line in Figure 2.2. The positive wave angle results in positive longshore current and sand transport to the west. The average values of the monthly mean wave height, period, and angle are about 0.6 m, 8 s, and 10°, respectively. These average values will be selected to represent constantly incident wave conditions for the computation of eroded beach recovery during 2015 – 2020 in Chapter 3.

2.3 Tide Gauge Data and Offshore Wave Data

Tide gauge data at Dauphin Island (Tide Station 8735180 in Figure 2.5) are available from the Center for Operational Oceanographic Products and Services at National Oceanic and Atmospheric Administration (NOAA 2021a). This tide station is located 13 km east of the study site. The mean high water, mean sea level, and mean low water based on the datum of NAVD88 are 0.207 m, 0.016 m, and -0.154 m, respectively. The water level data were collected at a sampling rate of 0.1 h.

Offshore wave data was obtained from the National Data Buoy Center of NOAA (NOAA 2021b). The wave gauge (NDBC Buoy Station 42012 in Figure 2.5) was

located in the depth of 23.5 m off the coast of Orange Beach, AL (57 km east of the study site). The data was available during 1983 – 1984 and after 2009 with the sampling rate of 1 h. The average values during 2015 – 2020 of the root-mean-square wave height H_{rms}, the spectral peak period T_p, and the peak spectral wave direction θ were 0.57 m, 5.4 s, and 6.2°, respectively. Major storm events since 2005 are tabulated in Table 2.2 together with the peak still-water elevation. The tide gauge data and wave data are used in the computation for Hurricane Nate in 2017 with the highest peak still-water level since 2009.

Figure 2.5 Locations of tide gauge and wave gauge near the study site

Table 2.2 Hurricanes with landfall date and peak water level recorded by tide gauge on Dauphin Island, Alabama

Hurricane	Landfall Date	Peak Water Level (m)
Katrina	29 August 2005	1.75
Ida	10 November 2009	0.99
Isaac	29 August 2012	1.14
Nate	8 October 2017	1.17
Sally	15 September 2020	1.10
Zeta	29 October 2020	0.94

Chapter 3

COMPUTATION OF ERODED BEACH RECOVERY

The dry beach width seaward of the rubble mound structure increased during 2015 – 2020 (Figures 2.1 and 2.2). The cross-shore numerical model CSHORE (Kobayashi 2016) is used to predict the process of the observed beach recovery. In this chapter, input to CSHORE for seven cross-shore line profiles is summarized. The computed seaward shoreline displacements are compared with the available measured data.

3.1 CSHORE Input

The shoreline measurement dates are tabulated in Table 3.1. The dates of 31 December 2015 and 30 November 2018 are added to output the annual shoreline variation. For brevity, use is made of t_0 = 0, t_1 = 365 d, t_2 = 731 d, t_3 = 1065 d, t_4 = 1430 d, t_5 = 1795 d, and t_6 = 2161 d. The initial beach profiles are extracted from the 2015 DEM data (Mickey et al. 2019) along the seven cross-shore lines (L1 – L7), as shown in Figures 2.3 and 2.4. In this recovery computation, the buried rubble mound in 2015 is neglected because of the expected increase of the dry beach width.

The time series of H_{rms}, T_p, and θ need to be specified at the seaward boundary in the water depth of about 6 m. For this initial attempt to reproduce the long-term shoreline recovery, constant representative waves are assumed and taken as H_{rms} = 0.6 m, T_p = 8 s, and θ = 10° based on the visual observations by Douglass (1994). The sensitivity of the computed shoreline recovery to the assumed waves is presented in

Section 3.4. The still water level is assumed zero (NAVD88) for this micro-tidal beach. It is noted that the use of constant water level and waves reduces numerical difficulties.

The median sand diameter is 0.37 mm. The specific gravity, porosity, and fall velocity of the sand are taken as 2.6, 0.4, and 0.051 m/s, respectively. The cross-shore nodal spacing is 2 m. The input parameters are taken as the standard values used in the previous beach erosion and recovery computations by Kobayashi and Jung (2012) who calibrated the bed load parameter B = 0.001 or 0.002. The computation time was 20 minutes for the computed duration of almost six years for each cross-shore line. The numerical efficiency of CSHORE allows a number of calibration and sensitivity computations.

Table 3.1 Dates of shoreline measurement and computation

Time	**Date**	**Number of Days**
t_0	1 January 2015	0
t_1	31 December 2015	365
t_2	31 December 2016	731
t_3	30 November 2017	1065
t_4	30 November 2018	1430
t_5	30 November 2019	1795
t_6	30 November 2020	2161

3.2 Seaward Shoreline Displacement

The computed seaward shoreline displacement Δx using B = 0.001 and B = 0.002 are shown as a function of the number of days for lines L1 – L7 under the assumption of alongshore uniformity (IQYDY=0) in Figure 3.1. The seaward shoreline displacement Δx is relative to the shoreline on 1 January 2015. Δx is positive (negative) for shoreline accretion (erosion). The decrease of the bed load parameter B reduces onshore sand transport and the seaward shoreline displacement. CSHORE predicts onshore bed load transport and offshore suspended load transport. The bed load transport rate is proportional to the value of B. Figure 3.1 indicates the importance of onshore bed load transport for beach recovery. In the following, B = 0.001 is adopted to reproduce the measured shoreline displacement and reduce small numerical fluctuations.

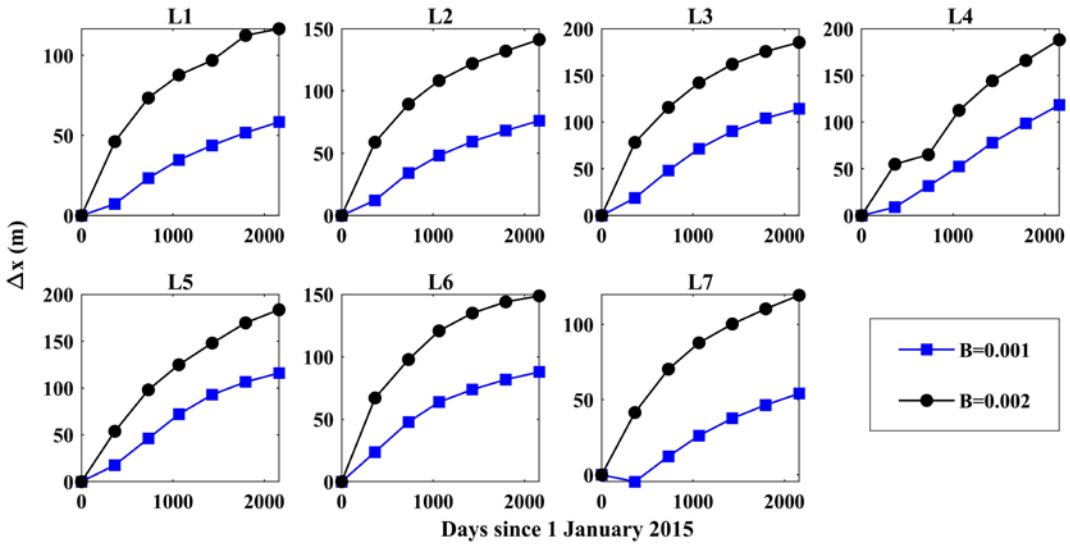

Figure 3.1 Computed seaward shoreline displacement Δx (m) as a function of the number of days since 1 January 2015 (Table 3.1) for lines L1 – L7 with Δx = 0 on zero day for bed load parameter B = 0.001 and 0.002

The computed shoreline displacements for IQYDY=0 in Figure 3.1 do not consider longshore sand transport gradient among L1 – L7. Zhu and Kobayashi (2021a) approximated the alongshore gradient of the longshore sediment transport rate per unit width, q_y, using the computed q_y on the given cross-shore line divided by the equivalent alongshore distance y_e, which was calibrated to account for alongshore sand loss or gain on the same cross-shore line. The computation for alongshore variability is denoted by IQYDY=1 which requires the input of y_e. The equivalent alongshore distance y_e may be related to Katrina Cut width of about 2 km. The calibrated value is y_e = 1,000 m to mimic the alongshore variability of Δx among L1 – L7. The computed seaward shoreline displacements for IQYDY=0 and 1 at time $t = t_0 - t_6$ are compared with the measured shoreline displacement at time $t = t_0$, t_2, t_3, t_5, and t_6 for lines L1 – L7 in Figure 3.2. The computed Δx for IQYDY=0 and B= 0.001 is too large except for L4 in the middle of the Katrina Cut. The computed Δx for IQYDY=1 with the calibrated y_e is similar to the measured Δx, implying the shoreline recovery due to onshore sand transport and net longshore sand transport toward L3, L4, and L5 with the measured Δx exceeding 50 m after 2161 days. However, detailed horizontal sediment transport processes are not computed by the cross-shore model CSHORE with the calibrated y_e.

Figure 3.3 shows the initial profile and computed profiles for IQYDY=0 and 1 as well as the measured shoreline location (cross) at end time $t = t_6$ for L1 – L7. The shoreline location is predicted better after the inclusion of the longshore sand transport gradient. The initial profiles in 2015 for L3, L4, and L5 included a terrace near the elevation of -2 m. This terrace may have been the remnant bottom of the channel breached by Hurricane Katrina in 2005 and is predicted to migrate landward under the

computed onshore sand transport. Figure 3.3 may indicate the importance of onshore sand transport for the recovery but no subaqueous profile data are available after 2015. The computed step is located at the seaward edge of irregular wave breaking under the assumed constant water level and waves. This step may be artificial. Sand transported landward of the step is mostly deposited and shifts the shoreline seaward for L3 – L 5. Sand transported toward the shoreline along L1, L2, L6, and L7 is removed by longshore sand transport for the case of IQYDY=1.

The computed onshore sand transport volume (including void) per unit width at the seaward boundary x = 0 (Figure 3.3) since 1 January 2015 are tabulated in Table 3.2 for IQYDY=0 and in Table 3.3 for IQYDY=1 and y_e = 1,000 m. The annual onshore sand transport volume is about 10 m^2/y at x = 0 and zero at the landward boundary x = 1,000 m. The computed rate at x = 0 is of the same order of magnitude as the computed rate by Kobayashi and Jung (2012) on Rehoboth and Dewey beaches in Delaware.

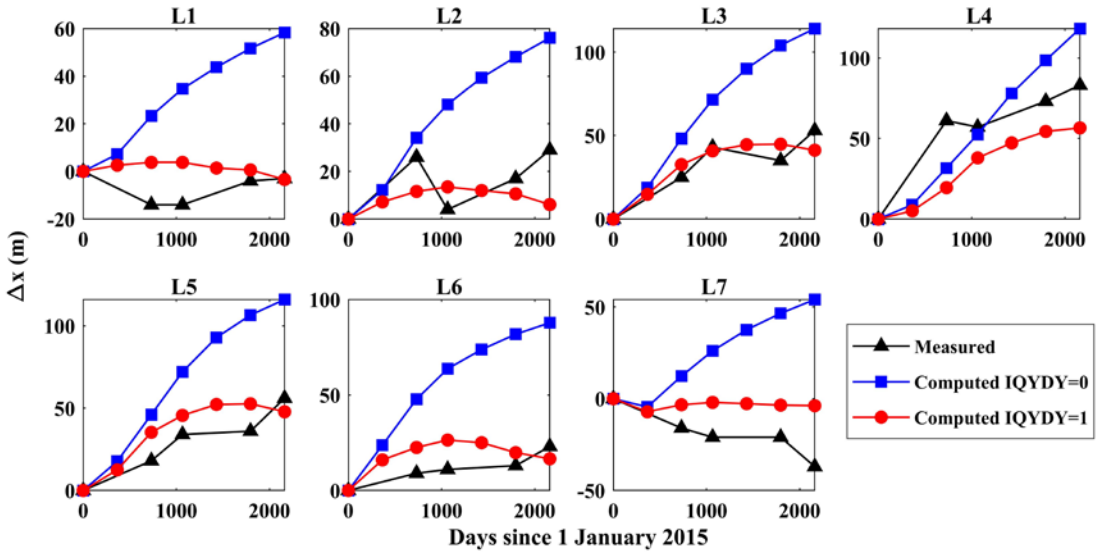

Figure 3.2 Computed shoreline displacement Δx (m) for alongshore uniform case (IQYDY=0) and alongshore gradient case (IQYDY=1 and y_e = 1,000 m) at time $t = t_0 - t_6$ for lines L1 – L7 as well as measured shoreline displacement at time $t = t_0$, t_2, t_3, t_5, and t_6 (Table 3.1)

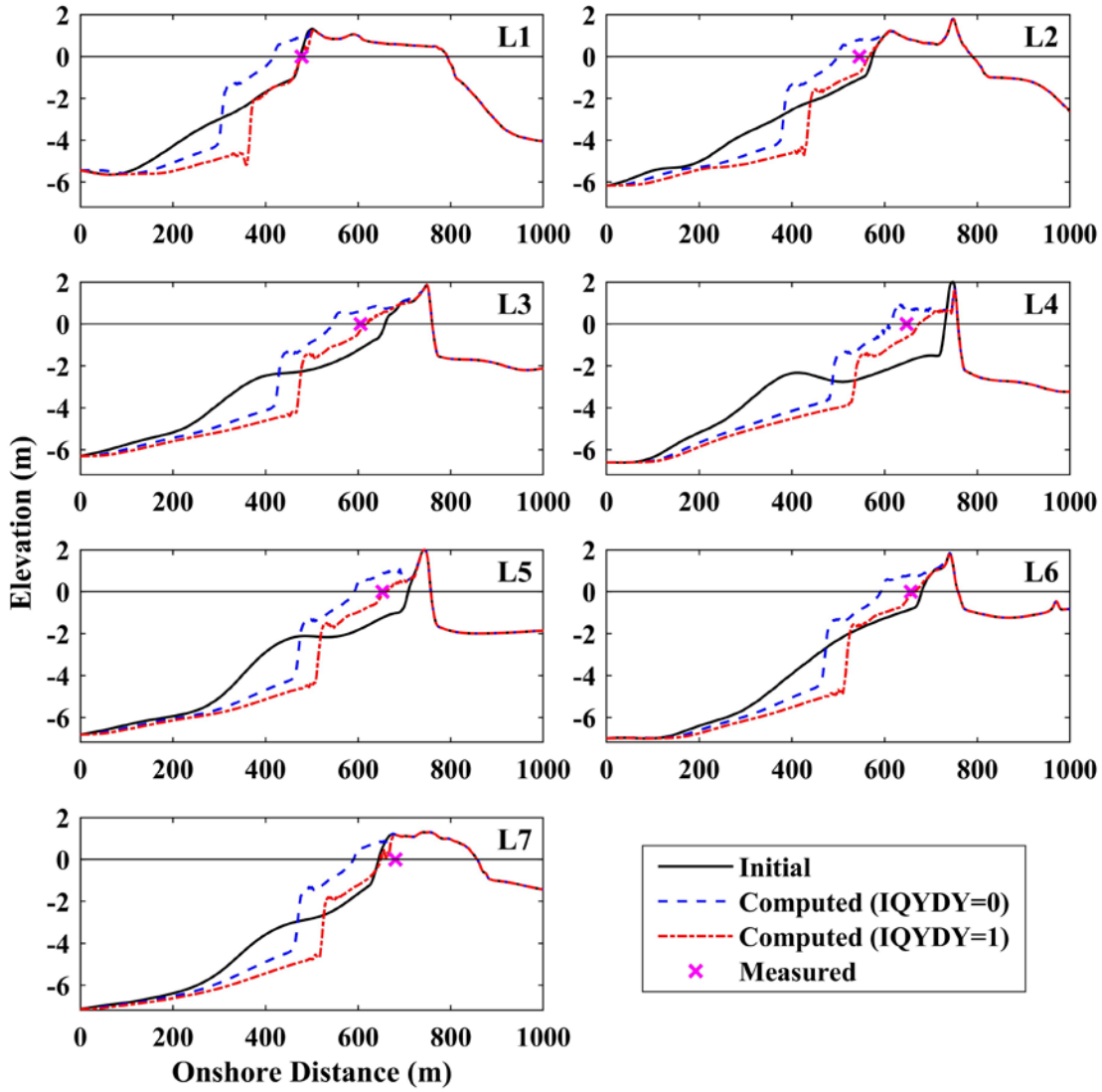

Figure 3.3 Initial and computed (IQYDY=0 and 1) profiles as well as measured shoreline location (×) at end time $t = t_6$ for lines L1 – L7

Table 3.2 Computed onshore sand tansport volumes (including void) per unit width at the seaward boundary x = 0 since 1 January 2015 for lines L1 – L7 where IQYDY=0 and B = 0.001

Time	Number of Days	Onshore sand transport volumes (m^3/m)						
		L1	**L2**	**L3**	**L4**	**L5**	**L6**	**L7**
t_1	365	10.2	7.7	7.4	6.7	6.2	5.9	5.6
t_2	731	20.4	15.5	14.8	13.4	12.4	11.7	11.2
t_3	1065	29.7	22.6	21.6	19.5	18.1	17.1	16.3
t_4	1430	39.8	30.3	29.0	26.1	24.3	22.9	21.9
t_5	1795	50.0	38.1	36.4	32.8	30.5	28.8	27.5
t_6	2161	60.1	45.9	43.8	39.5	36.7	34.7	33.1

Table 3.3 Computed onshore sand tansport volumes (including void) per unit width at the seaward boundary x = 0 since 1 January 2015 for lines L1 – L7 where IQYDY=1 and B = 0.001

Time	Number of Days	Onshore sand transport volumes (m^3/m)						
		L1	**L2**	**L3**	**L4**	**L5**	**L6**	**L7**
t_1	365	10.2	7.7	7.4	6.7	6.2	5.9	5.6
t_2	731	20.4	15.5	14.8	13.4	12.4	11.7	11.2
t_3	1065	29.7	22.6	21.6	19.5	18.1	17.1	16.3
t_4	1430	39.8	30.3	29.0	26.1	24.3	22.9	21.9
t_5	1795	50.0	38.1	36.4	32.8	30.5	28.8	27.5
t_6	2161	60.2	45.9	43.8	39.5	36.7	34.7	33.1

3.3 Longshore Sand Transport Rate

The annual longshore sand (including void) transport rate Q_y (m^3/y) is computed for each cross-shore line as shown in Figure 3.4. The cumulative longshore sand transport volume is obtained by integrating the longshore sand transport rate q_y from time $t = 0$ to arbitrary t and from $x = 0$ to $x = 1{,}000$ m. The computed cumulative volume as a function of time t is divided by the duration t and converted to the annual rate Q_y which may be compared with the annual rate of the order of 10^5 m^3/y estimated by Douglass (1994). The temporal variation of Q_y under constant water level and waves is related to computed beach profile evolution which is smaller along the edge lines L1 and L7 and larger along the center lines L3, L4, and L5. The computed Q_y may approach constant when the eroded beach recovers fully.

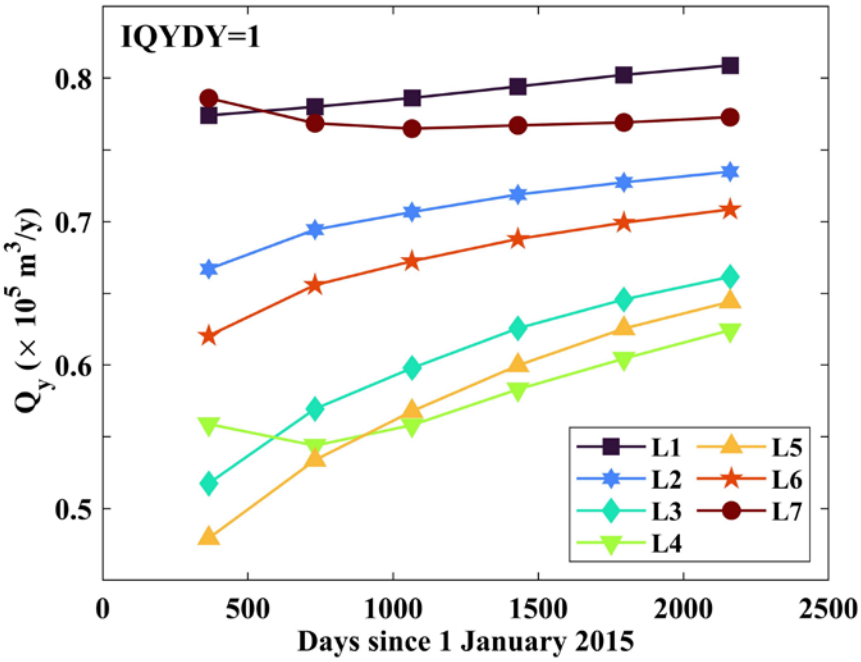

Figure 3.4 Longshore sand transport rate Q_y of the order of 10^5 (m^3/y) at time $t = t_1 - t_6$ using computed cumulative longshore sand transport volume (including void) in the computation domain of x = 0 – 1,000 m

3.4 Sensitivity of Computed Recovery to Representative Waves

The gross simplification of the representative waves for the shoreline recovery may be tolerable if the computed recovery is not very sensitive to the assumed constant waves. The computed results so far are limited to the incident waves represented by $H_{rms} = 0.6$ m, $T_p = 8$ s, and $\theta = 10°$. The monthly average wave conditions near the study site presented by Douglass (1994) suggest the wave heights, periods, and angles in the ranges of 0.4 – 0.8 m, 6 – 10 s, and 5° – 15°, respectively. In the following, the computed shoreline displacements for three different values of H_{rms}, T_p, and θ are presented one by one. The sensitivity to the representative sediment diameter is discussed at the end. The computed shoreline displacements are limited to IQYDY=1 with y_e = 1,000 m.

3.4.1 Sensitivity to wave height

The sensitivity to the root-mean-square wave height $H_{rms} = 0.4$, 0.6, and 0.8 m for $T_p = 8$ s and $\theta = 10°$ is shown in Figure 3.5. The representative wave height $H_{rms} = 0.6$ m does not give the best agreement of all the seven lines. The agreement for L7 is the best for $H_{rms} = 0.8$ m. The agreement for L5 is slightly better for $H_{rms} = 0.4$ m. The computed shoreline displacement is accretional (positive) and roughly similar for $H_{rms} = 0.4$ and 0.6 m but can become erosional (negative) for $H_{rms} = 0.8$ m. The larger H_{rms} at the seaward boundary $x = 0$ increases the irregular breaking wave height, suspended sand volume per unit bottom area, and offshore suspended sand transport by undertow current in the surf zone (e.g., Kobayashi 2016). The accretional and erosional trends on this beach with the median sand diameter $d_{50} = 0.37$ mm are similar to those on the beaches in Delaware with $d_{50} = 0.33$ mm computed by

Kobayashi and Jung (2012). The average value of H_{rms} was 0.59 m for the accretional period of 221 days and 0.81 m for the erosional period of 51 days.

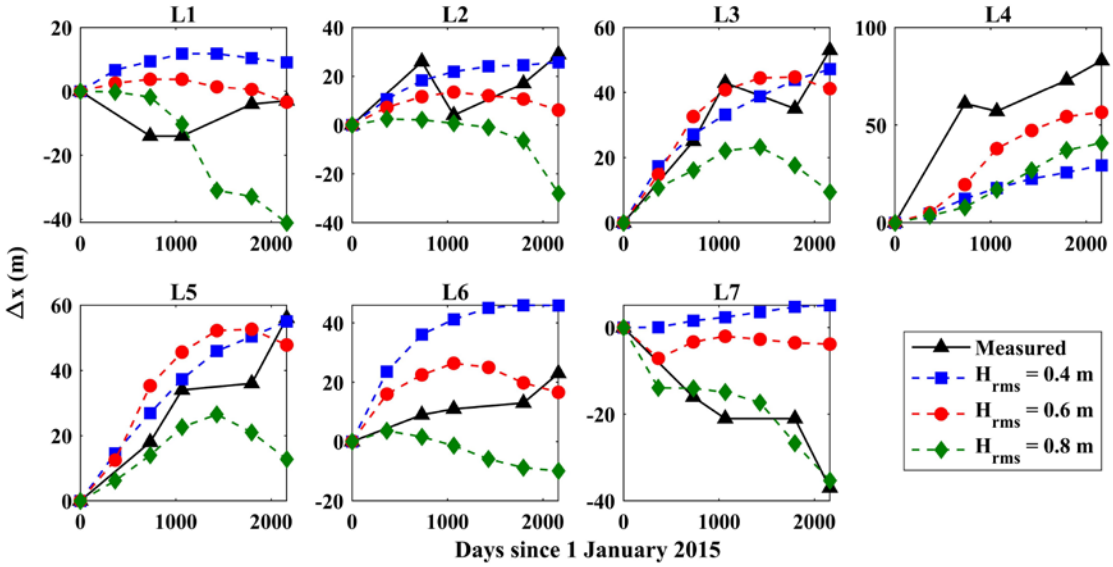

Figure 3.5 Computed shoreline displacement Δx (m) for root-mean-square wave height H_{rms} = 0.4, 0.6, and 0.8 m at time $t = t_0 - t_6$ for lines L1 – L7 as well as measured shoreline displacement where T_p = 8 s, θ = 10°, and IQYDY=1

3.4.2 Sensitivity to wave period

Figure 3.6 depicts the sensitivity to the spectral peak period T_p = 6, 8, and 10 s for H_{rms} = 0.6 m and θ = 10°. The ranges of the computed values of Δx for the seven cross-shore lines (L1-L7) in Figure 3.6 are less than the corresponding ranges in Figure 3.5. The computed shoreline displacement is not very sensitive to the representative wave period T_p. No single value of T_p gives the best agreement for all the seven lines.

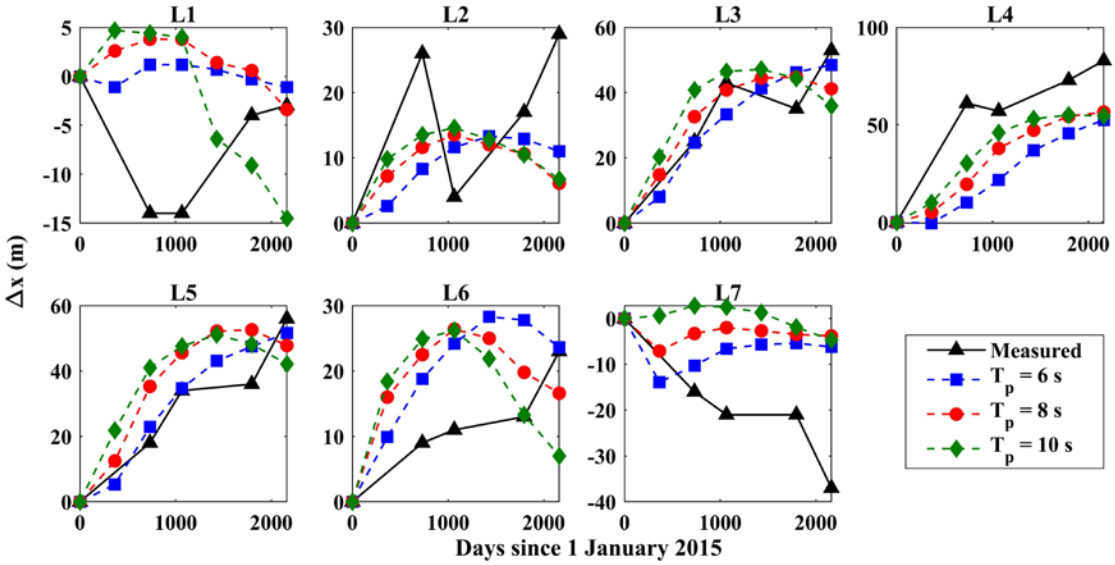

Figure 3.6 Computed shoreline displacement Δx (m) for spectral peak period T_p = 6, 8, and 10 s at time $t = t_0 - t_6$ for lines L1 – L7 as well as measured shoreline displacement where H_{rms} = 0.6 m, θ = 10°, and IQYDY=1

3.4.3 Sensitivity to wave angle

Figure 3.7 shows the sensitivity to the peak spectral wave direction $\theta = 5°$, 10°, and 15° for $H_{rms} = 0.6$ m and $T_p = 8$ s. The accretional shoreline displacement decreases with the increase of the wave angle θ because the longshore sand transport rate q_y increases with the increase of θ. For the case of IQYDY=1 with the alongshore gradient of q_y, the equivalent alongshore distance y_e has been calibrated as $y_e = 1{,}000$ m. The local bottom elevation change with time is determined by the cross-shore gradient of the cross-shore sediment transport rate q_x and the longshore gradient of q_y which was approximated as q_y/y_e. This implies that the increase of q_y can be compensated by the increase of y_e. The calibrated value of $y_e = 1{,}000$ m is specifically for the representative waves of $H_{rms} = 0.6$ m, $T_p = 8$ s, and $\theta = 10°$.

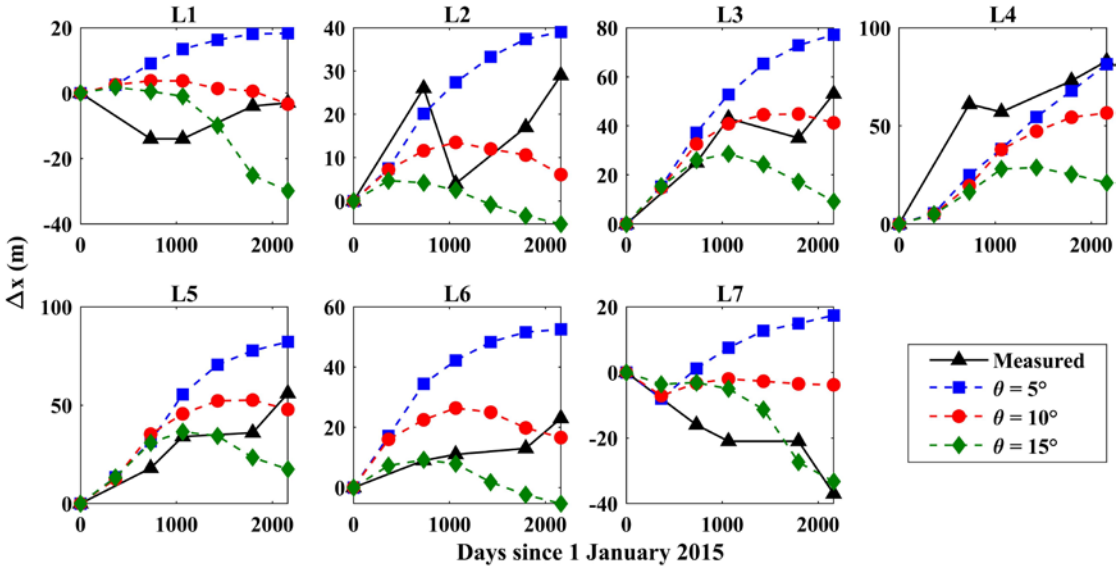

Figure 3.7 Computed shoreline displacement Δx (m) for peak spectral wave direction θ = 5°, 10°, and 15° at time $t = t_0 - t_6$ for lines L1 – L7 as well as measured shoreline displacement where H_{rms} = 0.6 m, T_p = 8 s, and IQYDY=1

The sensitivity of the longshore sand transport rate Q_y plotted in Figure 3.4 is also examined for L4, as indicated in Figure 3.8. The effect of T_p on Q_y is relatively small, as in Figure 3.6. The computed Q_y increases with the increase of H_{rms} and θ as expected from the Coastal Engineering Research Center (CERC) formula (USACE 2003). Figures 3.5 – 3.7 suggest that the uncertainties associated with the representative waves may produce 100% uncertainty of the computed shoreline displacement which is comparable with the 100% error of the sediment transport model in CSHORE (Kobayashi 2016). The use of representative waves is convenient for field sites with limited wave data.

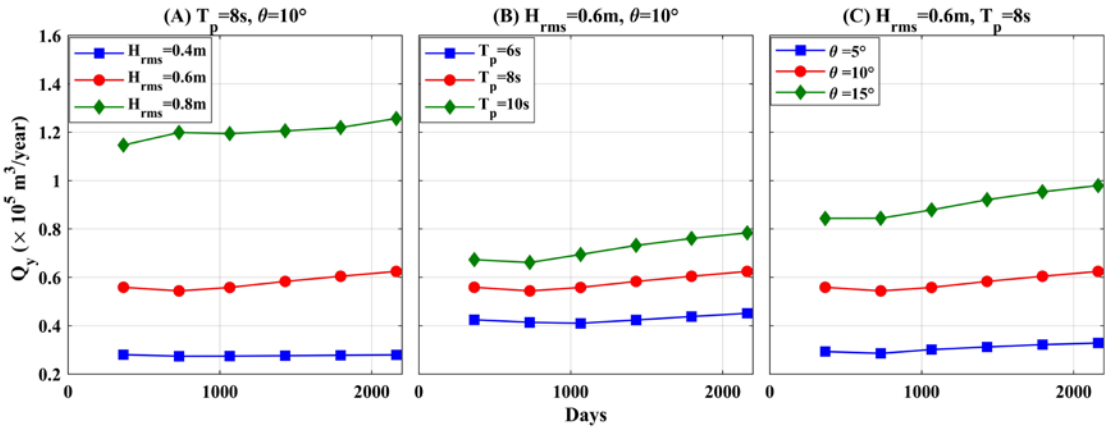

Figure 3.8 Longshore sand transport rate Q_y of the order of 10^5 (m^3/y) at time $t = t_1 - t_6$ for L4 where (A) H_{rms} = 0.4, 0.6, and 0.8 m; (B) T_p = 6, 8, and 10 s; (C) θ = 5°, 10°, and 15°

3.4.4 Sensitivity to sediment diameter

The sediment diameter d_{50} is 0.37 mm in the vicinity of the Katrina Cut and in the range of 0.28 – 0.43 mm on the beaches east of the Katrina Cut (Douglass 1994). Figure 3.9 shows the sensitivity to d_{50} = 0.28, 0.37, and 0.43 mm for H_{rms} = 0.6 m, T_p = 8 s, and θ = 10°. The estimated fall velocities for the sand with d_{50} = 0.28, 0.37, and 0.43 mm are 0.036, 0.051, and 0.062 m/s, respectively. The computed accretional shoreline displacement Δx decreases with the decrease of the sand diameter d_{50} except for L5 and d_{50} = 0.43 mm at time $t = t_2$ and t_3 (see Table 3.1) because of the increase of suspended sand volume and offshore suspended sand transport. For d_{50} = 0.28 mm, the values of Δx became negative (erosional) except for L4 with its initial shoreline on the rubble mound. The seaward shoreline displacement for L4 and d_{50} = 0.28 mm was zero because the rubble mound structure was not eroded. These sensitivity computations start from the initial profiles of L1 – L7 in 2015 for d_{50} = 0.37 mm. The initial profiles for d_{50} = 0.28 and 0.43 mm could be different. Nevertheless, Figure 3.9 indicates the importance of the sand diameter for the recovery of the eroded beach.

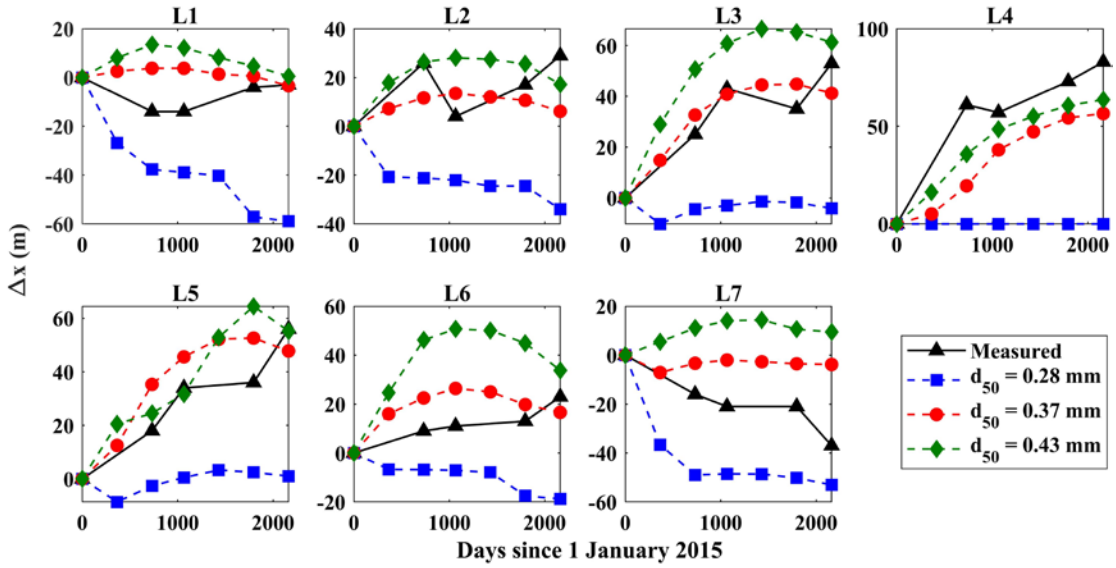

Figure 3.9 Computed shoreline displacement Δx (m) for sediment diameter d_{50} = 0.28, 0.37, and 0.43 mm at time $t = t_0 - t_6$ for lines L1 – L7 as well as measured shoreline displacement where H_{rms} = 0.6 m, T_p = 8 s, and IQYDY=1

Chapter 4

COMPUTATION FOR HURRICANE NATE

In this chapter, the effect of the beach width on the Katrina Cut rubble mound structure during major storms is assessed for line L4 with the largest recovery of 83 m depicted in Figure 3.3. Computations were made for Hurricane Nate in 2017 with the highest peak still-water level since 2009 (Table 2.2) and a hypothetical storm to reproduce the still water level of Hurricane Katrina in 2015.

4.1 Computation Domain and CSHORE Input

The wave gauge located 57 km east of L4 is used to estimate the offshore waves in the water depth of 23.5 m. The computation domain of $x = 0$ – 1,000 m in Figure 2.3 is extended offshore by 5,100 m using a bottom slope of 1/300 (vertical/horizontal). The new computation domain of $x = 0$ – 6,100 m starts from the water depth of 23.5 m at $x = 0$. The computed results near the Katrina Cut structure are essentially the same for the domain extended using the slope of 1/150 – 1/300. The tide gauge located 13 km east of L4 is used to estimate the still water level. The waves near the shoreline are limited by depth-limited wave breaking. The time series of the still-water elevation, root-mean-square wave height H_{rms}, spectral peak period T_p, and wave angle θ shown in Figure 4.1 are used as the seaward boundary conditions for line L4. The 72-h hourly time series started from 7 October 2017, one day before the landfall date of Hurricane Nate in Table 2.2. The time of the peak still-water level is indicated by a vertical line in Figure 4.1. The computed results for IQYDY=0 and 1 were found to be almost the

same but the value of y_e is uncertain for Hurricane Nate. The computed results for IQYDY=0 (no y_e) are presented in the following.

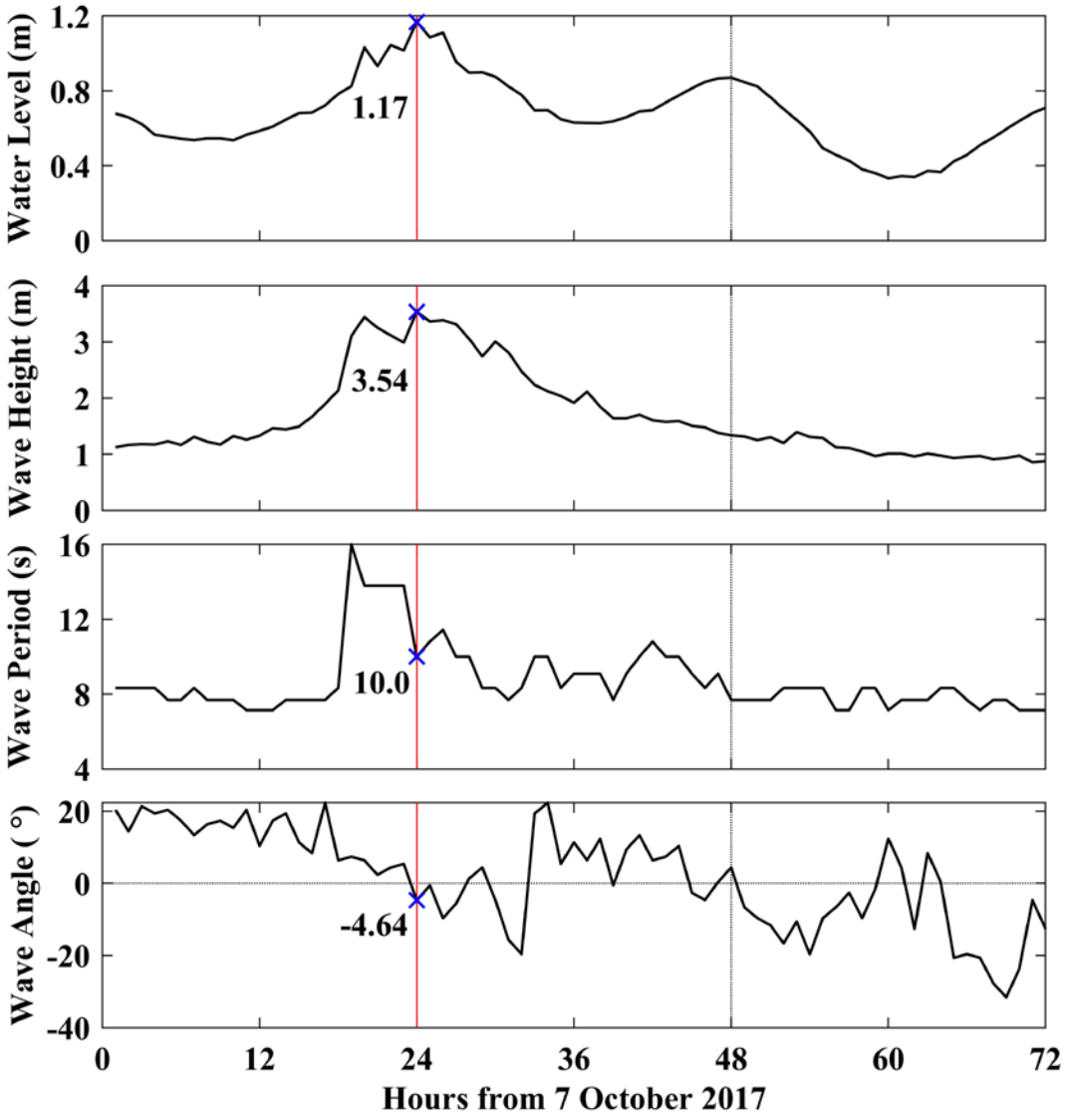

Figure 4.1 3-day time series of still-water elevation at tide gauge and the wave height H_{rms}, peak period T_p, and angle θ at wave gauge during Hurricane Nate where the water level peaked on 8 October 2017 (Table 2.2)

4.2 Beach Profile Evolution

The rubble mound structure with the seaward and landward slopes of 1/2 (vertical/horizontal) described by Gonzalez et al. (2020) is incorporated in the cross-shore beach profile along line L4 because the structure can be exposed to wave action during Hurricane Nate. The crest and base widths of the rubble mound are 6.1 m and 22 m, respectively. The crest and toe elevations (NAVD88) are 2 m and -2 m, respectively. The nominal diameter, density, and porosity of the rock are 0.55 m, 2.6 g/cm^3, and 0.44, respectively. Four initial profiles along line L4 were investigated to examine the effect of recovering beach conditions on the rubble mound: (A) the hypothetical profile in 2011; (B) the surveyed profile in 2015; (C) the computed profile in 2017; and (D) the computed profile in 2020.

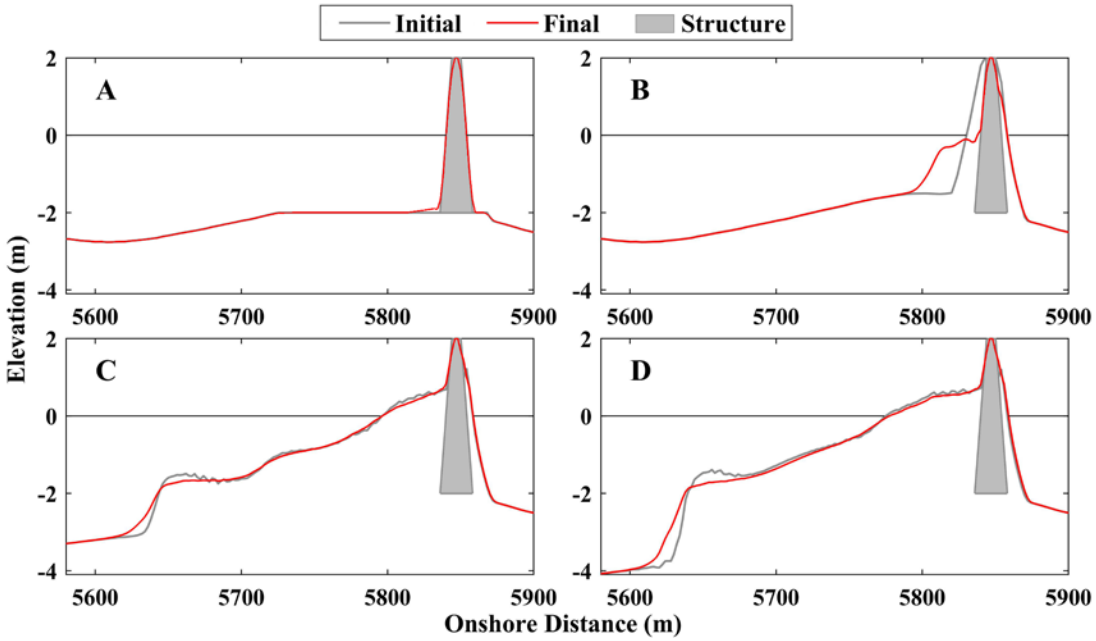

Figure 4.2 Initial profiles (A: hypothetical profile in 2011 after the rubble mound construction; B: measured profile in 2015; C: computed profile in 2017; D: computed profile in 2020) and computed final eroded profiles at the end of Hurricane Nate where the grey trapezoid indicates the rubble mound

The hypothetical profile in 2011 refers to the breached beach profile just after the structure construction obtained by removing sand above -2 m of the surveyed profile in 2015. The computed profiles are stored during the recovery simulation to obtain the 2017 profile on the starting day of Hurricane Nate and the 2020 profile at the end time t_6 (Figure 3.3). The initial and final profiles at time $t = 72$ h of discernible profile change in the zone of $x =$ 5550-5900 m are presented in Figure 4.2 where the grey trapezoidal part is the cross-section of the rubble mound structure. The rock units are assumed to be stationary in this simulation of the beach profile change (Kobayashi and Kim 2017). No sand was present inside the 2011 rubble mound (A), whereas sand was assumed to cover the entire rubble mound in 2015 (B), 2017 (C), and 2020 (D). The 2011 profile mimicking the breached beach is predicted to be stable during the hurricane. Visible erosion is computed on the sand covered slope of the 2015 rubble mound. The eroded sand is predicted to be deposited on the fronting beach at the elevation near -2 m. For the 2017 and 2020 profiles with the recovered dry beach, the artificial step created by the representative waves is predicted to be eroded during the hurricane.

The root-mean-square wave height H_{rms} was obtained by multiplying the computed free-surface standard deviation σ_η by $2\sqrt{2}$. The computed H_{rms} for four profiles in the range of x = 5,100 – 5,900 m at time t = 24, 48, and 72 h are shown in Figure 4.3. Wave height decreased sharply at $x \approx$ 5,840 m because wave breaking on the rubble mound structure. The wide dry beach between x = 5,650 – 5,840 m in 2017 (C) and 2020 (D) profiles reduced the wave height gradually in front of the rubble mound structure.

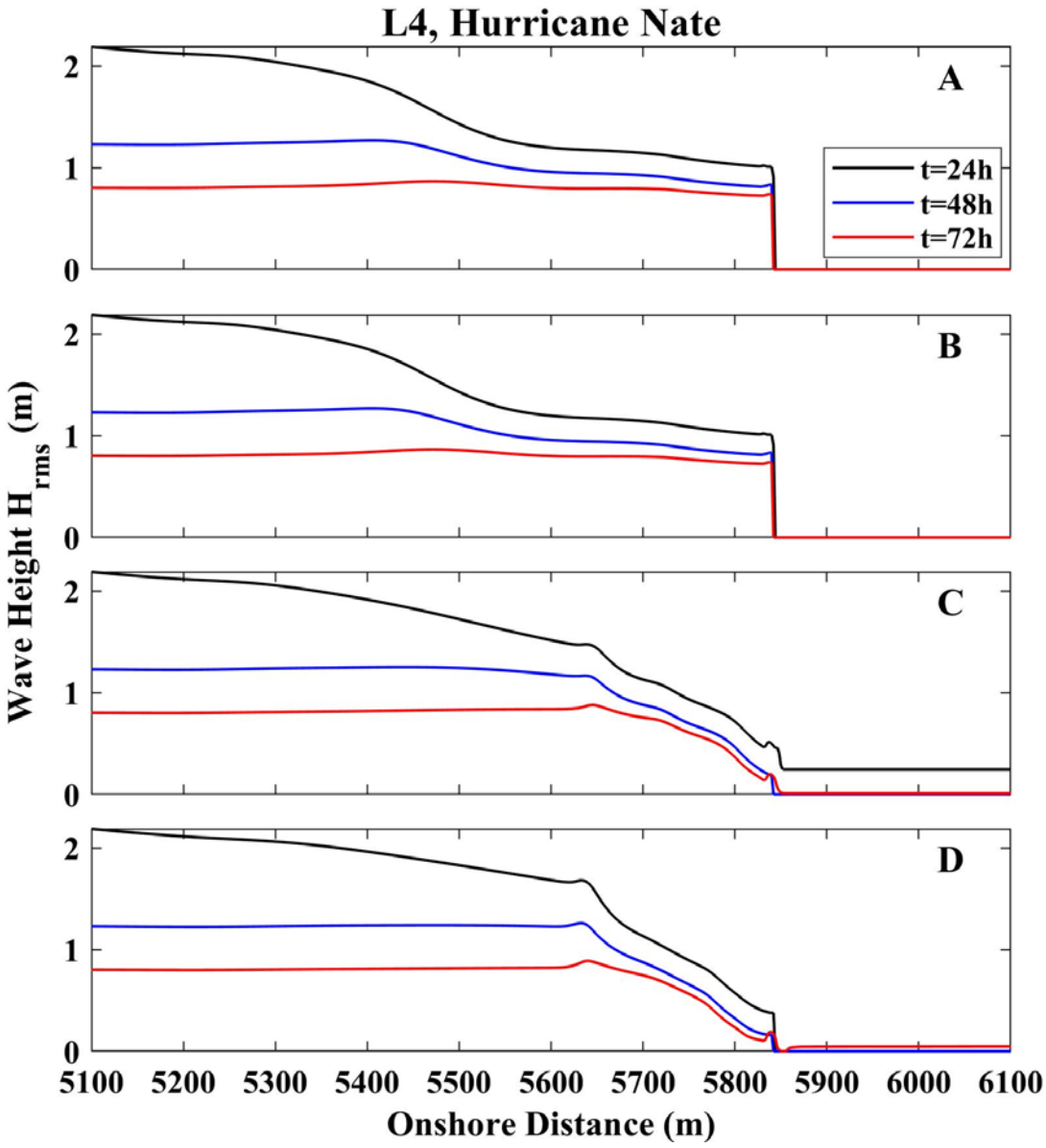

Figure 4.3 Computed root-mean-square wave height H_{rms} at time t = 24, 48, and 72 h for four initial profiles during Hurricane Nate

4.3 Damage Progression

Damage progression of a rubble mound structure during storms needs to be predicted for the structure design (Melby and Kobayashi 2011). The experiment by Zhu and Kobayashi (2021b) indicated little protection of a sand mound by a destroyed rock cover. The rubble mound deformation during Hurricane Nate is computed for the fixed initial beach profiles in Figure 4.2. CSHORE cannot compute sand and rock movement simultaneously. No sand is assumed to exist inside the rubble mound above the fronting sand beach elevation so that armor rock units are exposed to direct wave action.

Damage is defined as $S = A_e/(D_{n50})^2$ where A_e is the eroded armor area computed by CSHORE and D_{n50} is the nominal rock diameter of 0.55 m. The input critical stability number N_c is taken as 0.7 and 0.1 for careful and casual rock placement, respectively (Kobayashi et al. 2010; Yuksel and Kobayashi 2021). The temporal variations of the computed damage progression for the four cases in Figure 4.2 during Hurricane Nate are plotted in Figure 4.4. The reduction of N_c from 0.7 to 0.1 causes increased damage for the 2011 and 2015 initial profiles (A and B). The 2016 visual observations by Gonzalez et al. (2020) suggested causal rock placement on this temporary structure. Damage progression is continuous for the most exposed case A in 2011 where the computed value of 3 for $N_c = 0.1$ at end time $t = 72$ h indicates cross-sectional damage of 3 rock units for the width of one rock diameter. For the less exposed case B in 2015, damage is computed to occur for seven hours near the peak still-water level at time $t = 24$ h (Figure 4.1). For the 2017 and 2020 profiles with the fronting dry beach, the computed damage is practically zero even for $N_c = 0.1$. This is consistent with little structure damage to the infrastructure observed after Hurricane Nate in 2017 (Coogan et al. 2019). The computed damage differences are related to the fronting beach elevations of -2.0 m, -1.5 m, 1.0 m, and 1.0 m in the 2011, 2015, 2017,

and 2020 profiles, respectively. The importance of the fronting beach elevation in reducing depth-limited breaking wave heights was stated by Gonzalez et al. (2020).

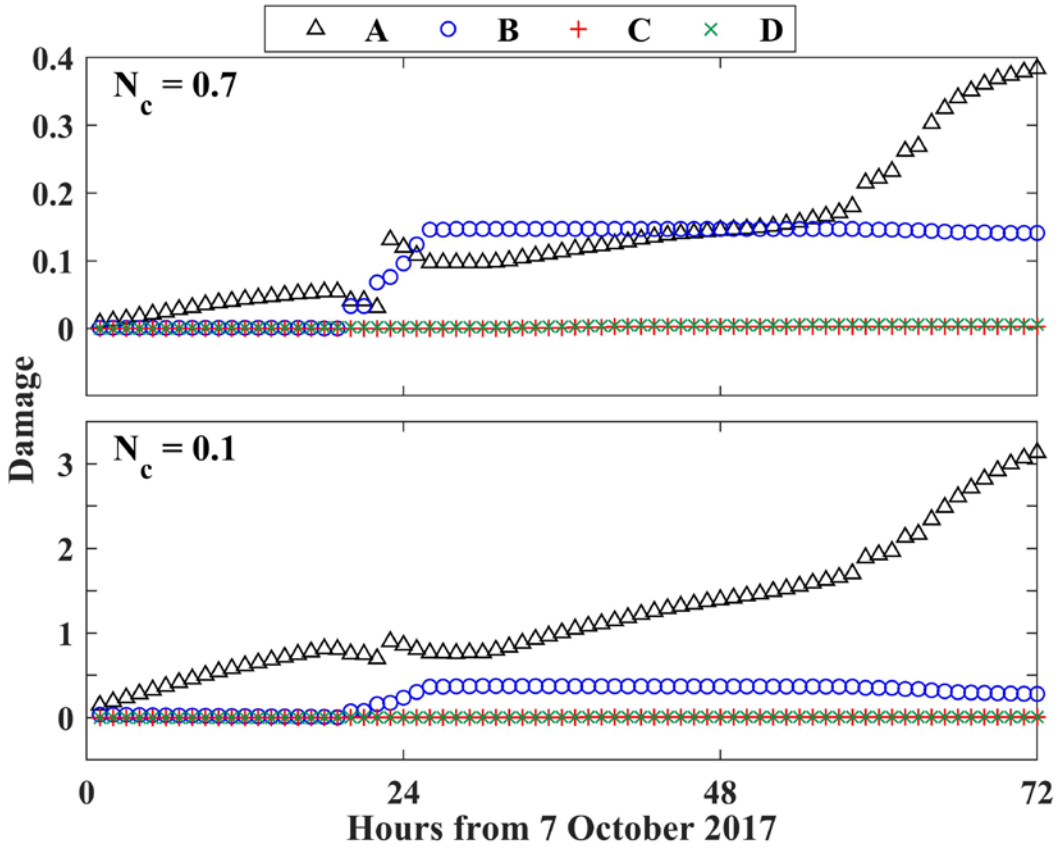

Figure 4.4 Computed damage of exposed armor rock layer above fronting sand beach during Hurricane Nate for critical stability number N_c = 0.7 and 0.1 corresponding to careful and casual rock placement, respectively, where the computed damage is almost the same for cases C and D

4.4 Hypothetical Storm NatePlus (Nate + 0.58 m)

Kobayashi and Zhu (2017) created a hypothetical Hurricane SandyPlus by increasing still water level to mimic the still water level of a 500-year storm and predicted the impact of wave overtopping of a barrier beach. In this study, computation was also made for a hypothetical storm, named NatePlus. The still water level in Figure 4.1 was increased by 0.58 m for the entire 72-h duration to produce the peak water level of 1.75 m of Hurricane Katrina (Table 2.2), which caused the Katrina Cut. The offshore wave conditions and four initial profiles are kept the same.

The computed profiles and damage progression for Hurricane NatePlus are compared with those of Hurricane Nate. Figure 4.5 shows the initial and computed final profiles at the end of Hurricane Nate and Hurricane NatePlus. The computed profile changes during Hurricane NatePlus increase somewhat in the vicinity of the rubble mound in comparison to those during Hurricane Nate. The computed damage for the 2011 and 2015 profiles is larger but the damage increment is less than about 1.2 (Figure 4.6). The computed damage for the 2017 and 2020 profiles remains small and is less than about 0.2. The water level increase of 0.58 m is predicted to increase the beach erosion and armor damage but the predicted increase is relatively minor, perhaps because of the Katrina Cut structure constructed in 2011 after Hurricane Katrina in 2005.

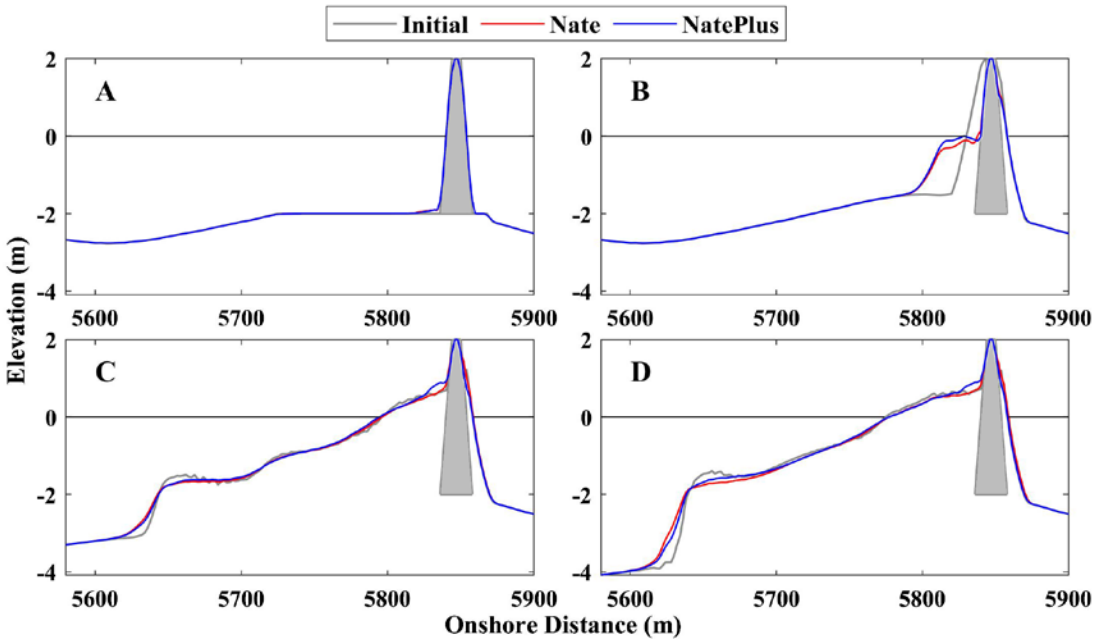

Figure 4.5 Initial and computed final eroded profiles at the end of Hurricane Nate and Hurricane NatePlus where the grey trapezoid indicates the rubble mound

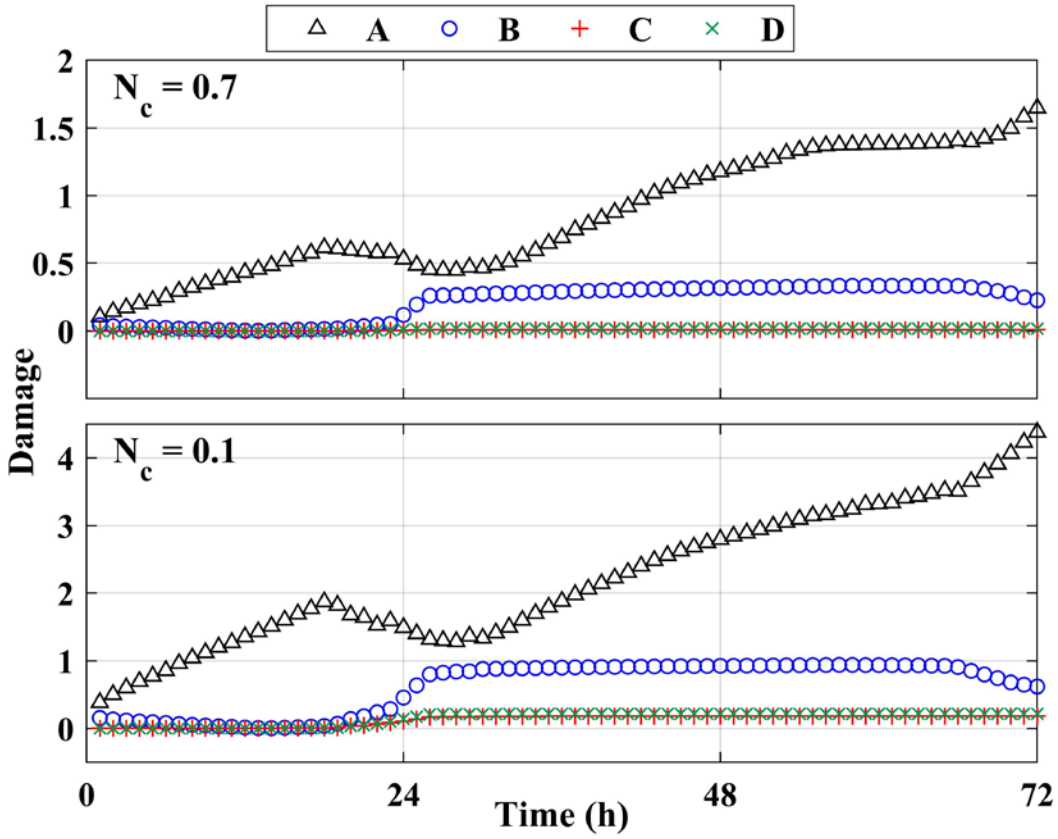

Figure 4.6 Computed damage of exposed armor rock layer above fronting sand beach during Hurricane NatePlus for critical stability number N_c = 0.7 and 0.1

Chapter 5

CONCLUSIONS

The rubble mound structure constructed in 2011 to close the channel in Dauphin Island breached by Hurricane Katrina in 2005 was investigated along seven cross-shore lines during 2015-2020 (almost six years) using the numerical model CSHORE. Constant representative waves are proposed to reproduce the recovering dry beach width seaward of the rubble mound structure. Onshore sand transport on the breached beach restores the dry beach width and longshore sand transport moves sand toward the breached channel. However, detailed horizontal sediment transport processes are not computed. The annual longshore sand transport rate is computed to be of the order of 10^5 m^3 per year. The longshore sand transport rate is smaller in the middle of the breached channel because of the narrower surf zone on the lower beach elevation. The sensitivity of the beach recovery to the assumed representative waves is examined to quantify the expected error of this convenient engineering approach. The estimated error of 100% is similar to the error of the sediment transport model in CSHORE. Furthermore, the recovery of the eroded beach is sensitive to the sand diameter.

The long-term recovery computation did not include the rubble mound structure and storm conditions. The beach profile changes and the rubble mound damage during Hurricane Nate lasting 3 days were computed for the cross-shore line of the largest recovery. The survey profile in 2015 and three possible profiles in 2011, 2017, and 2020 were used as the initial profiles. The erosional profile changes during the stormy 3 days were much smaller than the accretional profile changes under the constant waves

lasting almost six years. The computed armor layer damage during Hurricane Nate in 2017 was negligibly small for the 2017 and 2020 beach profiles with the recovering wide beach. The computed damage became noticeable for the 2015 profile with a narrow dry beach and exceeded 3 for the hypothetical 2011 profile just after the rubble mound construction. The construction of the Katrina Cut structure initiated natural recovery processes of sand transport. In return, the recovering beach dissipates storm waves and reduces wave action on the structure.

REFERENCES

Coogan, J.S., Webb, B.M., Smallegan, S.M., and J.A. Puleo. 2019. "Geomorphic changes measured on Dauphin Island, AL, during Hurricane Nate." *Shore and Beach,* 87(4): 15–22. http://doi.org/10.34237/1008742.

Douglass, S.L. 1994. "Beach erosion and deposition on Dauphin Island, Alabama. U.S.A." *J. Coastal Research,* 10(2): 306–328. https://www.jstor.org/stable/4298218.

Froede, C. R. 2008. "Changes to Dauphin Island, Alabama, brought about by Hurricane Katrina (29 August, 2005)." *J. Coastal Research*, 24(4C): 110–117. https://doi.org/10.2112/06-0782.1.

Gonzalez, V.M., Garcia-Moreno, F.A., Melby, J.A., Nadal-Caraballo, N.C., and E.S. Godsey. 2020. *Alabama Barrier Island Restoration Assessment life-cycle structure response modeling.* Report ERDC/CHL TR-20-5. Vicksburg, MS: U.S. Army Engineer Research and Development Center, 91p.

Kobayashi, N. 2016. "Coastal sediment transport modeling for engineering applications." *J. Waterway, Port, Coastal, Ocean Eng.* 142(6): 03116001. https://doi.org/10.1061/(ASCE)WW.1943-5460.0000347.

Kobayashi, N., Farhadzadeh, A. and J.A. Melby. 2010. "Wave overtopping and damage progression of stone armor layer." *J. Waterway, Port, Coastal, Ocean Eng.* 136(5): 257–265. https://doi.org/10.1061/(ASCE)WW.1943-5460.0000047.

Kobayashi, N., and H. Jung. 2012. "Beach erosion and recovery." *J. Waterway, Port, Coastal, Ocean Eng.* 138(6): 473–483. https://doi.org/10.1061/(ASCE)WW.1943-5460.0000147.

Kobayashi, N., and H.D. Kim. 2017. "Rock seawall in the swash zone to reduce wave overtopping and overwash of a sand beach." *J. Waterway, Port, Coastal, Ocean Eng.* 143(6): 04017033. https://doi.org/10.1061/(ASCE)WW.1943-5460.0000416.

Kobayashi, N., and T. Zhu. 2017. "Bay flooding through tidal inlet and by wave overtopping of barrier beach." *J. Waterway, Port, Coastal and Ocean Eng.* 143(5): 04017024. https://doi.org/10.1061/(ASCE)WW.1943-5460.0000403.

Melby, J.A., and N. Kobayashi. 2011. "Stone armor damage initiation and progression based on the maximum wave momentum flux." *J. Coastal Research,* 27(1): 110–119. https://doi.org/10.2112/JCOASTRES-D-09-00122.1.

Mickey, R.C., Jenkins, R.L., Dalyander, P.S., Thompson, D.M., Plant, N.G., and J.W. Long. 2019. *Dauphin Island decadal forecast evolution model inputs and results.* U.S. Geological Survey data release, https://doi.org/10.5066/P9PDM1OJ.

Mickey, R.C., Godsey, E., Dalyander, P.S., Gonzalez, V., Jenkins, R.L., III, Long, J.W., Thompson, D.M., and N.G. Plant. 2020. *Application of decadal modeling approach to forecast barrier island evolution, Dauphin Island, Alabama.* U.S.

Geological Survey Open-File Report 2020-1001, 45 p., https://doi.org/10.3133/ofr20201001.

National Oceanic and Atmospheric Administration (NOAA), 2021a. Tides & Currents - Water Levels - 8735180 Dauphin Island, AL. https://tidesandcurrents.noaa.gov/waterlevels.html?id=8735180 (accessed October 2021).

National Oceanic and Atmospheric Administration (NOAA), 2021b. National Data Buoy Center - 42012 Orange Beach, 44 NW SW of Mobile, AL. https://www.ndbc.noaa.gov/station_page.php?station=42012 (accessed October 2021).

Passeri, D.L., Long, J.W., Plant, N.G., Bilskie, M.V., and S.C. Hagen. 2018. "The influence of bed friction variability due to land cover on storm-driven barrier island morphodynamics." *Coastal Eng.*, 132: 82–94. https://doi.org/10.1016/j.coastaleng.2017.11.005.

Roelvink, D., Reniers, A., Van Dongeren, A.P., De Vries, J.V.T., McCall, R. and J. Lescinski. 2009. "Modeling storm impacts on beaches, dunes and barrier islands." *Coastal Eng.* 56: 1133–1152. https://doi.org/10.1016/j.coastaleng.2009.08.006.

USACE (U.S. Army Corps of Engineers). 2003. *Coastal engineering manual.* Washington, DC.

Webb, B.M., Douglass, S.L., Dixon, C.R., and B. Buhring. 2011. "Coast guards." *Civil Engineering Magazine*, 81(12): 76–83. https://doi.org/10.1061/ciegag.0000378.

Yuksel, Z. T., and N. Kobayashi. 2020. "Comparison of revetment and sill in reducing shore erosion and wave overtopping." *J. Waterway, Port, Coastal, Ocean Eng.* 146(1): 04019028. https://doi.org/10.1061/(ASCE)WW.1943-5460.0000543.

Zhu, T., and N. Kobayashi. 2021a. "Modeling of soft cliff erosion by oblique breaking waves during a storm." *J. Waterway, Port, Coastal, Ocean Eng.* 147(4): 04021009. https://doi.org/10.1061/(ASCE)WW.1943-5460.0000642.

Zhu, T., and N. Kobayashi. 2021b. "Rock mound to reduce wave overwash and crest lowering of a sand barrier." *Coastal Eng. J.* 63(4): 504–516. https://doi.org/10.1080/21664250.2021.1957550